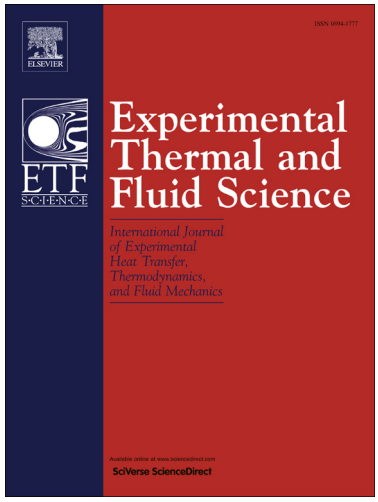

Investigation on bathtub vortex flow field by Particle Image Velocimetry

L. Cristofano, M. Nobili, G.P. Romano, G. Caruso

PII: S0894-1777(15)00348-9
DOI: http://dx.doi.org/10.1016/j.expthermflusci.2015.12.005
Reference: ETF 8648

To appear in: *Experimental Thermal and Fluid Science*

Received Date: 15 June 2015
Revised Date: 4 December 2015
Accepted Date: 5 December 2015

Please cite this article as: L. Cristofano, M. Nobili, G.P. Romano, G. Caruso, Investigation on bathtub vortex flow field by Particle Image Velocimetry, *Experimental Thermal and Fluid Science* (2015), doi: http://dx.doi.org/10.1016/j.expthermflusci.2015.12.005

Investigation on bathtub vortex flow field by Particle Image Velocimetry

L. Cristofano[1], M. Nobili[1], G.P. Romano[2], G. Caruso[1]

[1] *Sapienza University of Rome, Department of Astronautical, Electrical and Energy Engineering, C.so Vittorio Emanuele II, 244 – 00186 Rome, Italy*

[2] *Sapienza University of Rome, Department of Mechanical and Aerospace Engineering, Via Eudossiana, 18 – 00184 Rome, Italy*

Abstract

An experimental investigation on bathtub vortices has been performed by using Particle Image Velocimetry (PIV). Velocity fields associated to the free surface vortex were obtained at three horizontal planes and four Reynolds numbers, i.e. between 2400 and 11000 (calculated with reference to the exit hole diameter and the mean exit velocity). Due to the unsteady behavior of the flow field, the vortex center positions have been identified and the vortex paths were reconstructed for all experiments. Average velocity fields have been calculated by aligning the vortex centers at each frame, in order to derive radial and tangential velocity profiles, to be compared at different Reynolds numbers and measurement planes. The results show that the radial motion assumes a potential behavior when it is near the exit hole, scaling quite well with the average exit velocity (thus with the corresponding Reynolds number). On the other hand, the tangential component is well approximated by the Rankine's flow potential solution only near the free surface, the tangential velocity peak increment not being linearly proportional to the outlet velocity. Vorticity fields and circulation profiles have been derived from the measured velocity fields and discussed. Turbulence fluctuations statistical analysis gives also evidence of a clear dependence on Reynolds number and distance from the exit hole.

1. Introduction

Free surface vortices frequently appear in many hydraulic devices, such as turbine and pump intakes, or industrial reservoirs. They are characterized by a global rotational motion of the fluid, with increasing tangential velocity towards the center of the converging fluid due to conservation of angular momentum, and by the typical gas-liquid interface deformation, caused by static pressure decreases. The appearance of free surface vortices is undesirable in engineering applications because of the related swirling flow which reduces the hydraulic devices

performances. Moreover, floating particles and gas bubbles can be entrained in the main vortex, thus increasing the damage risk on moving parts of pumps and turbines. Besides this, gas entrainment (GE) phenomena due to free surface vortices represent a fundamental problem also from a safety point of view in nuclear industry, and in particular for Sodium-cooled Fast Reactors (SFRs). Actually, whirlpool formation in the upper tank of this kind of reactors could drag covering gas from the top of the vessel into the lower plenum, and then within the reactor core, thus resulting in undesirable and dangerous reaction product enclosure and reactivity effects. Therefore, a better understanding of such phenomena is required from both basic research and applied engineering systems point of views [1], [2].

Different researchers tried to develop analytical models and solutions describing steady free surface vortices, but the coupled treatment of a complex flow field with the gas-liquid interfaces makes very difficult to derive an exact analytical solution. Rankine [3] provided a simple mathematical description for the tangential velocity of the flow, which is characterized by a forced vortex in its central core, surrounded by a free potential vortex. The first exhaustive theoretical vortex model was proposed by Burgers [4] by considering a steady, axi-symmetric, laminar, unbounded flow and vortices with a negligible depth. The velocity field is obtained as an exact solution of Navier-Stokes equation, and it is valid near the vortex axis. These assumptions limit the applicability of Burgers' model to the conditions in which the free surface is not largely deformed. Moreover, the expression of Burgers' tangential velocity contains an exponential term still not solved in closed-form, so it does not allow the computation of vortex circulation. Rosenhead [5] proposed a different formulation for tangential velocity, easier to integrate, and Hite and Mih [6] derived the three velocity components expressions of the free surface vortex, by modifying the coefficient in Rosenhead's formula to match experimental data. The limits of this model are that the tangential and radial velocities are independent from the axial coordinate, whereas the modified coefficient strictly depends on experimental conditions. To solve these aspects, Chen et al. [7], starting from experimental measurements, provided a vortex model in which the three velocity components are functions of both radial and axial coordinates.

A more consistent vortex theory was suggested by Lundgren [8], who analyzed the problem of a bathtub vortex in a rotating container, by linearizing the dimensionless Navier-Stokes equation. Andersen et al. [9] first discussed the flow structure of a vortex in a rotating container, by distinguishing different flow regions, and by applying the Lundgren's model for describing the central free surface depression, also including the effects of surface tension and viscosity in the Ekman layer near the outlet orifice [10]. The same approach was used by Stepanyants and Yeoh [11], for the non-rotating case, by studying different regimes, i.e. whirlpools with different depth.

Even though this method provides a better description of the structure and the flow field of a free surface vortex, it is difficult to derive an exact analytical solution even for simple geometries, because of the mathematical complexity. Asymptotic analytical solutions are only possible for small-dent Burgers-Rott vortices, as derived by Stepanyants and Yeoh [12], but not for strong whirlpools. Therefore, it is not useful for engineering applications where boundary conditions and device geometries are often complex. This leads to the requirement of accurate numerical simulations and experimental measurements in such a flow field.

Several experimental investigations, aimed reproducing the free surface vortex formation and evolution, as well as identifying the underlying physical phenomena, were carried out in the last fifty years. Gulliver and Rindels [13] carried out experimental tests with the aim of predicting the formation of weak free surface vortices at vertical intakes with a headrace channel. In order to avoid whirlpool formation, they derived operability ranges of values for the main parameters as for example approach flow angle, intake submergence, intake velocity and length/width ratio of the headrace. Empirical correlation to demonstrate that surface tension effects are important for GE occurrence with unstable gas core were experimentally derived by Baum and Cook [14], using sodium, water, white spirit and Freon 113 as working fluids. Caruso et al. [15] performed experimental tests and preliminary observations by varying the water level, the flow rate and the outlet tube diameter in a small facility to classify the observed phenomena and obtain vortex occurrence maps. Cristofano et al. [16] discussed the aforementioned occurrence maps and carried out a dimensionless analysis to identify the most important dimensionless parameters (Reynolds, Froude and Weber numbers) that influence the physical phenomenon. They identified empirical correlations for the transition boundaries between stages. The most critical issue of these kind of studies is that the obtained maps and empirical correlations, are strongly dependent on the specific experimental conditions (geometry and scale of the facility, operating fluid physical properties, mass flow rate and submergence levels), so that is highly questionable their generalization. This surely requires a more general comprehension of the phenomenon.

From the numerical simulations point of view, many authors performed single phase (Sakai et al. [17]) or two-phase (Ito et al. [18]) flow computations, also with turbulence models (Merzari et al. [19]), to verify that single phase simulations allow at identifying the velocity field only far from the free surface. Škerlavaj et al. ([20], [21]) tested the Monji et al. benchmark case [22] with single-phase CFD simulations, concluding that the Shear-Stress-Transport with curvature correction (SST-CC) and the Scale Adaptive Simulation with curvature correction (SAS-CC) turbulence models can both be used for correct predictions of free surface vortices. Cristofano et al. [23] analyzed the vortex formation transient, by testing several numerical methods for the evaluation of the free surface vortex gas core length (L_{gc}). The main limit of these investigations

is that simpler models are not suitable to numerically reproduce vortex formation and evolution, while more complex models have been tested only for simple cases since they require high computational costs.

In last years, the use of Particle Image Velocimetry (PIV) improved a lot the direct measurement of velocity fields aiming to reveal the flow structure in free surface vortices. Noguchi et al. [24] by measuring the velocity field by means of PIV in a rotating cylindrical tank, concluded that experimental results are in good agreement with Rankine's analytical model only when the suction rate is large, the conservation of angular momentum in radial direction being not good for weak suctions. Kimura et al. [25], also using PIV, identified two different GE mechanisms, one due to von Karman vortex type at wake regions, and the other caused by an interacting shear flow, but the structure of occurred vortices was not analyzed. PIV measurements of Li et al. [26] allowed to compare the tangential and radial velocity distribution at different vortex stages, and to compute the circulation radial profile. In all these studies PIV measurements have been performed only on a single horizontal plane and the flow field at different heights has not been investigated. Monji et al. [22] performed PIV measurements on horizontal and vertical planes observing that in case of high water level and high flow rate, downward velocity gradient was constant and close to that used in the Burgers vortex model. Cristofano et al. [27] used PIV measurements to validate different analytical vortex models (i.e. Burgers', Hite's and Chen's) by comparing tangential and radial velocities and vorticity distributions. Results confirmed that the Hite's model has the better agreement with the experimental data concerning tangential velocity and vorticity.

In the present paper a first PIV measurement campaign, performed on the above described flow field, is presented and the results are discussed. The aim of this study is to characterize the structure of unforced free surface vortices, generated in a non-promoting test section geometry, by measuring velocity fields at different horizontal planes and by analyzing the flow field variations along the axial coordinate. PIV measurements have been carried out for different vortex stages, varying the Reynolds number in the outlet hole, in order to highlight any modification of the flow field with the vortex strength. Radial and tangential average velocity fields have been evaluated in steady-state conditions (time averaged). Compared to previous measurements performed by Monji et al. [22] and Cristofano et al. [27], in the present study the spatial dependence of radial and tangential velocity components is analyzed in detail. In particular, measurements have been carried out taking special attention to the near exit hole and to the free surface regions, comparing experimental data with the potential flow solutions. Trajectories of the vortex center have been reconstructed; in addition, characteristic times of vortex precession have been evaluated to identify possible periodicity of the vortex position

around the exit hole. Moreover, the statistical parameters of turbulence (Root Mean Square - RMS - of radial and tangential velocities) have been calculated. Experimental data obtained from this study could be very useful to validate analytical models and numerical methodologies used through computational fluid-dynamics tools. Moreover, it could be very interesting to compare the present results with the flow field of a "forced vortex", generated for example by introducing a tangential flow inlet.

2. Experimental setup

2.1. Experimental facility

In Fig. 1, the layout of the GETS (Gas Entrainment Test Section) facility is shown. It consists of a test section, a pump, a magnetic flow meter, a regulation valve, three shut-off valves, pipes and fittings. The facility is characterized by a closed loop to obtain steady state test conditions. Starting from the pump, water flows through the flow meter (measured flow rate range: 0.05-0.23 kg/s, with an accuracy of 0.75% of the measured value) and a regulation valve before entering into the test section.

The PPMA test tank is 700 mm × 500 mm × 500 mm (H×L×W) with transparent walls 20 mm thick. The test section is characterized by a rectangular shape to avoid any forced rotation within the fluid and two symmetrical inlet nozzles to avoid asymmetric and perturbed flow introduction. A PMMA outlet pipe is connected at the center bottom of the tank; in the present tests an inner diameter D=0.026 m was used.

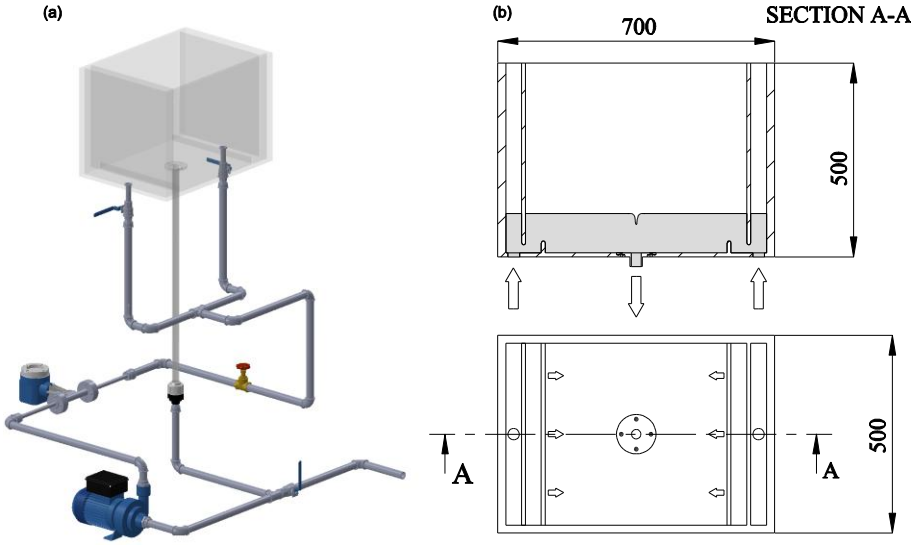

Fig. 1 a) 3D model of the test section. **b)** Vertical section and plant of the tank

Since upward inlet flows could perturb the free surface, especially at higher flow rates or at low fluid level, two vertical baffles and two other small septa are placed near the inlet holes to limit possible perturbations. Therefore, the two symmetric inlet flows lose their kinetic energy in the two volumes between the tank walls and the baffles before entering in the "active zone" of the test section.

PIV measurements have been carried out at the Fluid-dynamics Laboratory of the Mechanical and Aerospace Engineering Department of the "Sapienza" University of Rome. Measurements at three horizontal planes and for four different flow rates, corresponding to the four different development stages of vortex (Table 1) have been performed. The water level H in the tank was fixed at 50 mm in all the experimental tests; this value of the water level H, as well as the value of the outlet pipe diameter D, has been chosen since more stable vortices were generated with these conditions. The investigated Reynolds number is between 2450 and 11260, the Froude number, calculated with the exit velocity U, and the water level H, is between 0.13 and 0.62.

Table 1 Development vortex stages and corresponding tested mass flow rates and Reynolds numbers

Vortex stage		Mass flow rate [kg s^{-1}]	Reynolds Number	Froude Number
Stage 1 (S1)	Surface swirl and very small dimple	0.05	≈ 2450	≈ 0.13
Stage 2 (S2)	Well-developed dimple	0.1	≈ 4900	≈ 0.27
Stage 3 (S3)	Bubble entraining core	0.2	≈ 9800	≈ 0.54
Stage 4 (S4)	Full air core	0.23	≈ 11260	≈ 0.62

Table 2 shows the elevation, from the tank bottom, of the horizontal measurement planes. For each plane an area of about 19 × 19 cm (about 7.3 D) was framed.

Table 2 Horizontal measurement planes

Laser plane ID	Plane elevation z [mm]	Dimensionless plane elevation $z^*=z/H$
Plane 1 (P1)	25	0.5
Plane 2 (P2)	35	0.7
Plane 3 (P3)	45	0.9

Each test condition has been identified as "SXPY", where X and Y are, respectively, the stage number and the measuring plane number.

A double pulsed Nd-Yag laser provided a 2 mm thick light plane. The characteristic wavelength of the laser was 532 nm, with 200 mJ per pulse and duration of the single pulse of 0.76 ms. The high speed camera was a 10-bit CMOS BW Photron ultima APX with 1024 × 1024 pixels resolution at 50 fps, equipped with a Nikon Nikkor 50mm f/1.8 camera lens. Camera and laser pulses were synchronized at 125 fps for the high flow rate tests (Re≈11260) and 50 fps for the others. Therefore, the interval time between the two laser pulses and, consequently between two successive images, was respectively 1/125 s and 1/50 s. A single frame was obtained from the cross-correlation of two single images resulting from each double pulse. The laser repetition rate of a double pulse was 5 Hz, the time resolution of the system, allowing a frame acquisition rate of 0.2 s. The total acquisition time for each test was 204 s (the maximum time allowable by the internal memory of the camera) corresponding to about 1000 images. Hollow glass spheres with a diameter of 10 μm were used as seeding.

All the internal surfaces of the tank were obscured using a black adhesive film, leaving the tank interior optically accessible only through a window on the frontal wall for laser entrance. The camera was placed above the tank and the whole experimental apparatus, including camera and laser, was covered with a black sheet, in order to reduce the reflection, enhancing image quality. When the laser sheet cuts the vortex air core, strong reflections occur at the interface between water and air. Near the free surface, reflections are even more relevant because the vortex air core is larger. These reflections introduce measurement errors that cannot be prevented; through a proper selection of image analysis parameters they can be minimized. Moreover, the deformation of the free surface causes a "lens effect" resulting in measurement errors near the vortex center. For all tests performed in this study, the vortex gas core was very thin and related errors due to light reflections were small, whereas measurement errors due to the "lens effect" affect a larger region around the vortex axis. However, this region does not extend beyond a radius of about 3 mm from the vortex center in the worst case.

2.2. Experimental procedure and data reduction

A specific procedure has been defined on the basis of a preliminary tests aimed at identifying the conditions to be used in PIV experiments. These tests showed that the initial conditions within the tank strongly affect the vortices formation (i.e. in the presence of a not negligible initial vorticity, vortices formation is facilitated). The experimental test procedure foresees, after a previous test or perturbation, a waiting time (not less than 10 minutes) to obtain zero velocity condition within the tank. The pump is turned on and additional waiting time (five minutes) is

needed to ensure that all disturbances due to the initial transient vanished. Then, PIV acquisitions have been performed by recording 1024 image couples.

Before images processing, the background subtraction has been applied, in order to reduce the background noise and enhancing quality. The PIV analysis has been performed in two iterations: the first one with a starting window size equal to 128 x 128 pixels with 75% overlapping, the second one with a starting window size 32 x 32 pixel and 50% overlapping. Therefore, the vector spacing was 16 pixels, corresponding to about 3 mm (0.115 D), and each frame consisting of a 63 x 63 matrix.

Although steady boundary conditions were imposed during experimental tests, the formed bathtub vortices were characterized by a significant unsteadiness, with consistent variation of their position and intensity. Therefore, before calculating averaged velocity field and all the derived physical quantities, the vortex center of each instantaneous velocity fields was determined through a two steps procedure. First step: the *Q* parameter (Hunt et al. [28]) is calculated in a sub-region centered in the calculated vortex center of the previous frame and the position of the *Q* maximum value is detected. The *Q* criterion is used to identify vortical structures in incompressible flows, defined by Eq. (1):

$$Q=\frac{1}{2}\left(\Omega_{ij}\Omega_{ij}-S_{ij}S_{ij}\right)=\frac{1}{4}\left(\Omega-S\right)>0 \tag{1}$$

where Ω is the magnitude of the vorticity rate and S is the magnitude of the strain rate. The criterion states that in a vortical structure the vorticity magnitude prevails over the strain-rate; furthermore, $Q > 0$ is a necessary condition for the low pressure in a vortical structure.

Second step: a narrower sub-region, centered in the maximum *Q* position, is considered to identify the vortex center has been identified in two different ways:

- for each row and column of the matrix the sum of tangential velocity components is made and the row and column with maximum values of these sums are assumed as vortex center coordinates;
- in the same sub-region, the position where velocity magnitude is minimum is identified and stored.

Among the two above identified vortex center positions, that one closest to the position of the *Q* maximum value is selected. The accuracy of the vortex center position is about ±4.2 mm (i.e. the diagonal of the square cell of the measurement grid).

The vortex center identification allowed recovering the vortex trajectory during the acquisition. For each test, average velocity fields, centered on the instantaneous vortex center position, are

calculated. Consequently, the average velocity field dimension is smaller than the original frames (63 x 63), because it corresponds to the intersection of the 1024 frames. Average velocity fields and other statistic parameters arising from them (like vorticity distributions and circulation profiles) were calculated assuming a cylindrical coordinate system referred to the actual center of the vortex. The RMSs of radial and tangential velocities were calculated for all tests.

3. Experimental results

In this section, the experimental results are presented and discussed, following the PIV data analysis procedure. At first, the trajectories of the vortices and their positions over time have been obtained. Afterwards, the average velocity fields (coupled with the vorticity distributions) and the radial and tangential velocity profiles are presented and their profiles compared with the potential flow solutions. The circulation profiles have been calculated and presented as a function of the radial coordinate. Lastly, the RMSs of each velocity component are reported in order to evaluate the effect of turbulence fluctuations.
The series of results presented in the figures, for a specific Reynolds number or plane height, have to be considered representative of the other experimental conditions.

3.1. Vortex motion

3.1.1. Vortex trajectories and precession

In Fig. 2 the vortex trajectories for the test condition S1 are presented for the three measurement planes; similar results have been recognized for the other test with different Reynolds number. Vortex positions were measured with a frequency of 5 Hz, averaged over 1 s, corresponding to about 3.61 integral time scales (D/U), and plotted each 3 s in the figure. The coordinates x^* and y^* are normalized with the exit pipe radius R. As the distance of the horizontal measurement plane from the exit hole is increased, the vortex shows an increasing radius of the orbital motion around the hole (the exit hole projection on the measurement plane is also represented). This is a consequence of the three-dimensional motion of the vortex that is similar on the different horizontal planes even if with different amplitudes of the orbits and it is not surprising since the vortex is anchored to the exit hole. For the last position, the radius of the vortex orbit is even larger than that of the exit hole and the motion attains a sort of precession with variable radius.

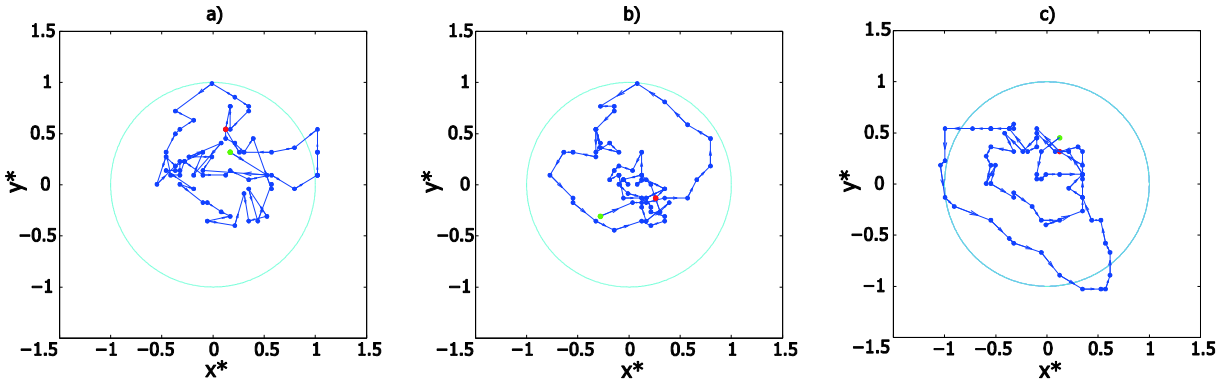

Fig. 2 Vortex trajectories with the sampling interval of 3 s: **a)** S1P1; **b)** S1P2; **c)** S1P3

It is important to investigate the effect on such vortex displacements due to changes in the flow rate. In Fig. 3 such a behavior is presented for the plane P3, showing that the smallest displacement occurs at an intermediate Reynolds number (S2). The amplitude of the vortex motion around the exit hole is initially decreasing (Figs. 3a and 3b) and then increasing (Figs. 3b, 3c and 3d). This strange behavior for the transition S1 - S2 has been observed also for the other two measurement planes and it can be explained by considering the effects of the vortex on the free surface corresponding to the two conditions.

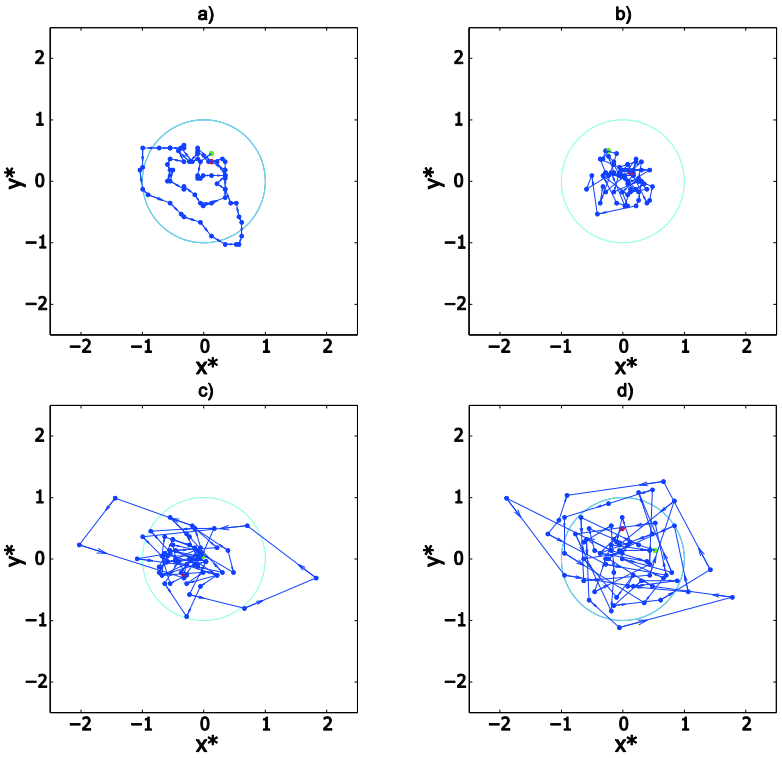

Fig. 3 Vortex trajectories with a sampling interval of 3 s for the higher plane at different flow rates: **a)** S1P3; **b)** S2P3; **c)** S3P3; **d)** S4P3

Specifically, as it can be seen from Fig. 4a, at Stage 1 (S1) the surface vortex is almost planar with a negligible free surface deformation. In this condition, the vortex is weakly anchored to the exit hole and its position is strongly affected by flow perturbations near the free surface. At Stage 2 (Fig. 4b), the free surface vertical deformation is not negligible. Therefore, the vortex structure is more rigid causing a more confined motion. At higher flow rates (i.e. S3 and S4, not shown here) the vortex structure is even more rigid, but unstable; it is characterized by larger variations in its intensity and large displacements of its trajectory. These qualitative observation have to be focused more deeply, by considering the variation in time of the vortex coordinate and the related characteristic amplitudes and time scales.

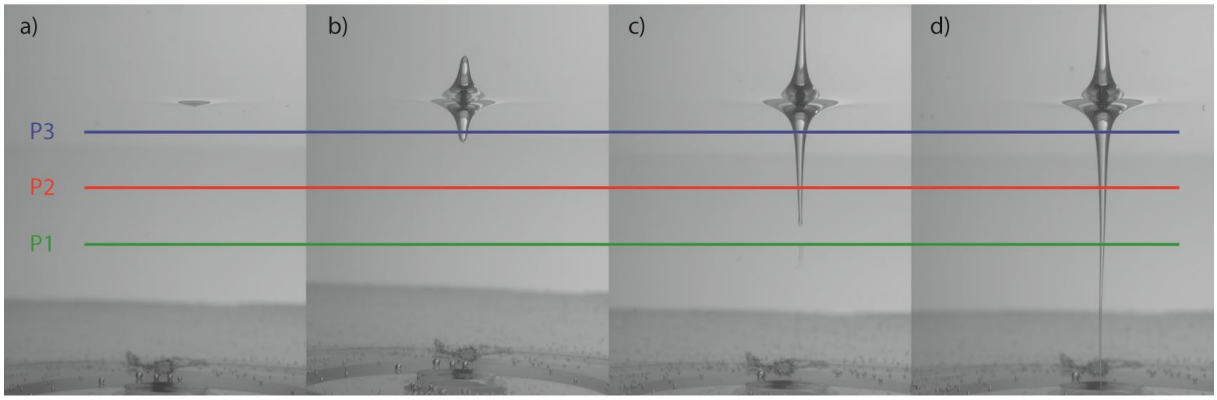

Fig. 4 Photos of free surface vortices: **a**) Stage 1,**b**) Stage 2, **c)**Stage 3, **d)** Stage 4

3.1.2. Vortex positions in time

The time behavior of the vortex center position along the x^*- coordinate relative to the center of the exit hole (non-dimensional by the exit pipe radius R) is presented for the stage S4 in Fig. 5 at different measurement planes. It is observed that both amplitudes and frequencies of oscillations are higher far from the exit plane; the same trend has been noticed for lower Reynolds numbers. Being the oscillations almost centered on the outlet hole (coordinate equal to zero), there is no bias towards a specified direction. A similar behavior, revealing an increment in amplitude and frequency of oscillations was also observed for increasing the flow rate. Similar results were noticed also for the y - coordinate.

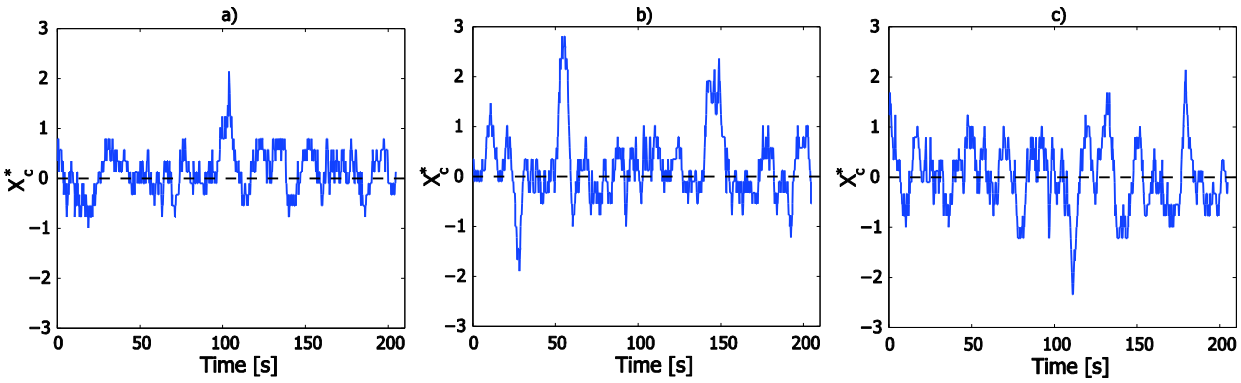

Fig. 5 Time behavior of normalized coordinate X_c/R of the vortex position: **a)** S4P1; **b)** S4P2; **c)** S4P3

In order to determine if those oscillations were regular or not and to characterize the vortex motion, the auto-correlation coefficients of vortex positions in time have been calculated. In almost all cases, excluding the peak at the starting time, there is a second peak in the interval 10 s to 80 s. This means that the moving vortices have trajectories recovering similar positions (from the statistical point of view) in time. This is especially evident for small flow rate regimes. From the correlation functions, a characteristic time scale of the flow field has been derived for radial and tangential coordinates of the vortex center, by evaluating the first peak in auto-correlation coefficients (excluding $t = 0$). These characteristic times were normalized by using the Strouhal number and analyzed in order to characterize the vortex wandering. This analysis was performed for both Cartesian (X_c,Y_c) and cylindrical (r_c,θ_c) coordinates of the vortex center; however, in both cases a definite behavior has not been found for tests at the same Reynolds number or at the same measurement plane. This would suggest that the vortex recover similar positions randomly in time.

3.2. Velocity field around the vortex

3.2.1. Average velocity fields

To determine a mean flow configuration, the average velocity fields have been computed from PIV measurements, by aligning the instantaneous vortex center positions at each frame, determined as in previous section, with the center of the average field. Therefore, 1024 double images have been used for each test to derive time-averaged velocity components $\bar{u}(x,y)$ in x- and $\bar{v}(x,y)$ in y - direction. Average errors in measurements are determined as in Eq. (2) by the

statistical error $\sigma_{u_j}^s$ on the velocity component u_j, which is proportional to the standard deviation σ_{u_j}:

$$\sigma_{u_j}^s(x,y)=\frac{2\cdot\sigma_{u_j}}{\sqrt{N}} \quad (2)$$

The computed average flow fields for two vortex stages (S1 and S3) and for two horizontal planes (P1 and P3) are presented in Fig. 6 in vector form, as a function of dimensionless coordinates. The background color indicates the magnitude of the vorticity component orthogonal to the plane, while the vector length is proportional to the velocity magnitude on the measurement plane. With reference to the vector field, at low flow rates (plots in the upper row of the figure) the vortex is small and well confined, as observed especially from the results on plane P1, which is closer to the hole outlet. On the other hand, at large flow rate (bottom row) the size and intensities of the vortex are much higher, involving a global motion in the whole acquisition region. As a consequence, velocity components are larger especially close to the free-surface (plot on the right part of the figure).

The vorticity contours in Fig. 6 (colored maps in background) clearly show the large vorticity near the vortex center. It seems that this region does not exhibit large variation in size at different measurement planes, while it increases at larger flow rates The larger values of vorticity are found at the larger flow rate and for the measurement planes closer to the free surface (case S3P3).

The average statistical error of tangential velocities is about 1.3%, with a maximum of 11.5%, while, concerning the radial velocities, the average statistical error is about 1.1%, with a maximum of 14%.

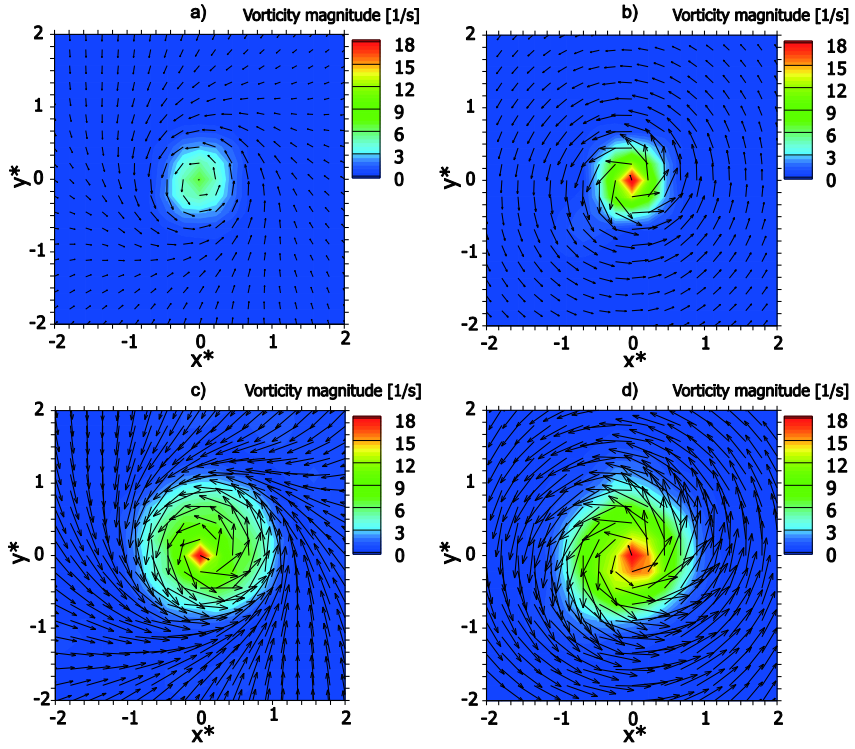

Fig. 6 PIV average velocity fields in vector form with vorticity magnitude contour for cases: **a)** S1P1; **b)** S1P3; **c)** S3P1; **d)** S3P3

3.2.2. Radial velocity profiles

Radial and tangential velocity profiles can be derived from these average fields and compared each other and with the potential flow theory, according to which radial velocity scales as *-1/r* and the tangential velocity scales as *1/r* (Rankine, 1858), being *r* the radial distance.

The velocity fields were transformed from the Cartesian coordinate system ($\bar{u}$,$\bar{v}$) to a polar coordinate system, to obtain tangential velocity $\overline{u_\theta}$ and radial velocity $\overline{u_r}$. Velocity profiles were derived from these average flow fields by the following azimuthal-average operation:

$$\left\langle \overline{u_\theta}(r) \right\rangle = \frac{1}{M}\sum_{i=1}^{M} \overline{u_{\theta_i}}(r,\theta)$$
$$\left\langle \overline{u_r}(r) \right\rangle = \frac{1}{M}\sum_{i=1}^{M} \overline{u_{r_i}}(r,\theta) \qquad (3)$$

Errors associated with these average values have been computed applying the error propagation law to measurement statistical error $\sigma_{u_j}^s$:

$$\sigma_{\langle \overline{u_j} \rangle} = \sqrt{\sum_{i=1}^{M} \left| \frac{\partial \langle \overline{u_j} \rangle}{\partial \overline{u_i}} \right|^2 \sigma_{\overline{u_i}}^{s\,2}} = \sqrt{\sum_{i=1}^{M} \left(\frac{\sigma_{\overline{u_i}}^s}{M} \right)^2} = \frac{1}{M}\sqrt{\sum_{i=1}^{M} \sigma_{\overline{u_i}}^{s\,2}} \qquad (4)$$

In Fig. 7, radial velocity profiles are presented for position P1 at different flow rates (Fig. 7a) and for case S1 at different planes (Fig. 7b). Velocity profile are normalized with the exit velocity U, while the radial coordinate is normalized with the exit pipe radius R ($r^*=r/R$). Here, radial velocities pointing toward the vortex center are defined as negative. It is important to point out that the radial velocity is fairly different from zero especially near the outlet (i.e. P1) and this is a clear indication of the fact that the fluid is coming out of the tank similarly to a sink configuration. All radial profiles are negative and are characterized by a minimum, except far from the hole (P3). Furthermore, as shown in Fig. 7a, it is evident that the normalized radial profiles, which are related to different flow rates, exhibit a good scaling behavior, being very close one to each other. Considering that P1 is the plane closer to the exit hole, this indicates that the radial flow is here governed predominantly by the exit fluid velocity U. Positive/negative peaks observed for $r^*\approx0$ are unphysical and caused by the lens effect due to the gas-liquid interface in the vortex. Moving closer to the free surface (as for position P3 in Figure 7b), the radial velocity assumes values close to zero and the whole radial profile is flat, thus meaning a vanishing role of the radial velocity.

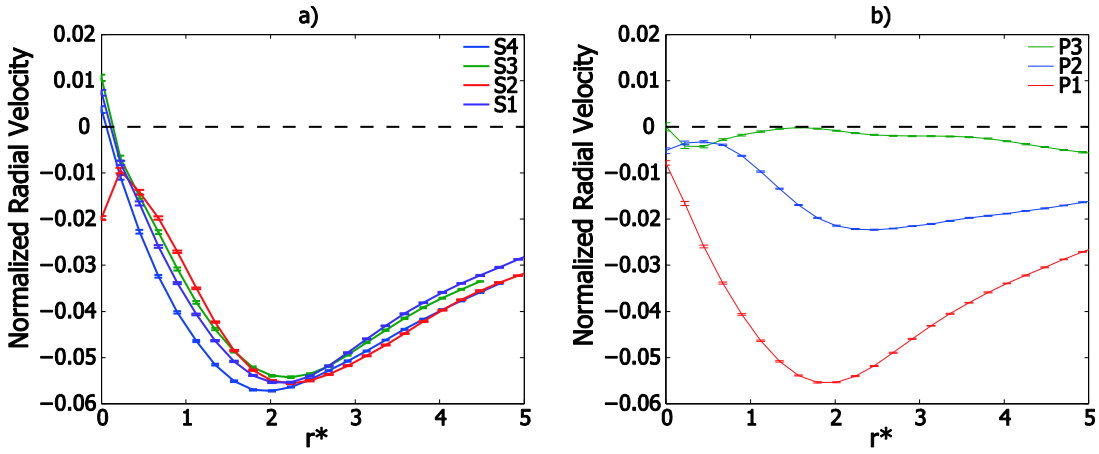

Fig. 7 Normalized radial velocity profiles: **a)** case P1 at different Reynolds numbers; **b)** case S1 at different planes

The average statistical error for the radial velocity measurement, calculated from the standard deviation of the 1024 frames, is about 4 %, reaching a maximum value of 13% for $r^*\approx0.45$; higher relative error are detected at lower r^* (near the vortex axis) as a consequence of the lens effect previously described.

The potential flow solution for radial velocity component for the simple sink case has the form of $-1/r$. For all test cases, the outer part of radial velocity profiles has been interpolated with the hyperbole equation

$$u_r = -\frac{a}{r} \tag{5}$$

In Table 3 are presented the *a* parameter values for the different test cases; it was not possible to interpolate radial velocity profiles with Eq. (5) for cases related to the plane P3, because of the very limited radial flow near the free surface. The coefficient *a* increases with Reynolds number and decrease moving far from the outlet.

Table 3 *a*-values for the different test cases

Test Case	$\boldsymbol{a}$ x 10^4 $[m^2\ s^{-1}]$	Test Case	$\boldsymbol{a}$ x 10^4 $[m^2\ s^{-1}]$
S1P1	1.75	S1P2	1.03
S2P1	4.12	S2P2	3.07
S3P1	7.29	S3P2	5.45
S4P1	9.04	S4P2	6.42

In Fig. 8, radial velocity profiles at P1 (Fig. 8a), and for cases S2 at different planes (Fig. 8b), are compared with potential flow trends. Radial velocity profiles related to the plane P1 are characterized by a decay very similar to the potential one, while the agreement with *–1/r* behavior worsens due to the positions closer to the free surface, P2 and P3 (for case S2P3 it was not even possible to drawn any potential trend).

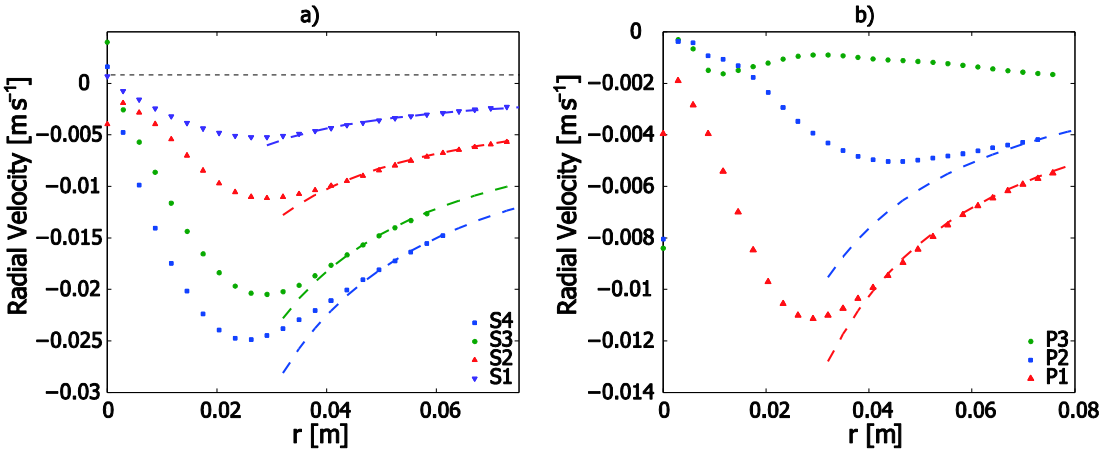

Fig. 8 Radial velocity profiles compared with potential behavior *-1/r*: **a)** case P1 at different Reynolds numbers; **b)** case S2at different planes

A preliminary analysis has been performed to find a functional dependence of the parameter *a* on Reynolds number and on z^*. Radial velocity component and radial coordinate in Eq. (6) have

been normalized, respectively, with the term $\sqrt{g\,H}$, where g is the gravity acceleration and H is the free surface level, and with the outlet tube radius R:

$$\frac{u_r}{\sqrt{g\,H}} = \frac{a'}{r} R \qquad a' = \frac{a}{R\sqrt{g\,H}} \tag{6}$$

Experimental data have been fitted using the following form:

$$a' = \alpha\, \mathrm{Re}^{\beta}\, z^{*\gamma} \tag{7}$$

As a result of the fit, the coefficients assume the following values:

$$\begin{aligned} \alpha &= 1.643\times10^{-6} \\ \beta &= 1.101 \\ \gamma &= -1.1 \end{aligned} \tag{8}$$

The correlation is characterized by a residual $R^2 = 0.983$ and an average percentage error of 6.85%; in Fig. 9 the experimental values of parameter *a'* are compared with the derived correlation (dashed lines describe the error boundaries of ±20%).

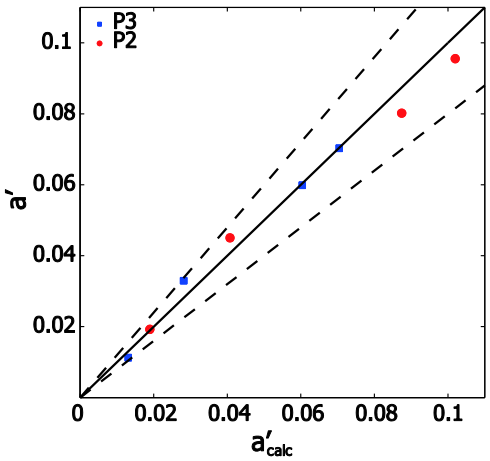

Fig. 9 Experimental vs calculated values of the parameter *a'*

Although this is a preliminary analysis, it can be noted that β and γ, which are respectively the exponent of Re and z^*, assume values closer to 1 (absolute value). This suggests that the parameter a is linearly dependent on the outlet mean velocity U and inversely proportional to the measurement plane height z, as already noticed. Thus, the experimental data have been fitted again with Eq. (7), imposing $\beta = 1$ and $\gamma = -1$; a different correlation has been obtained, with the coefficient α equal to 4.2×10^{-6}:

$$a' = 4.2\times10^{-6}\,\frac{\mathrm{Re}}{z^*} \tag{9}$$

This correlation presents statistics similar to the former correlation, with a residual $R^2 = 0.991$ and an average percentage error of about 8.3 %.

Nothing can be said now about the influence of exit hole diameter *D*, since all present experimental tests have been carried out with a single diameter.

3.2.3. Tangential velocity profiles

In Fig. 10, the tangential velocity profiles are presented at P3 and different flow rates (Fig. 10a) and for S1 at different planes (Fig. 10b). Velocity profile are normalized with the outlet velocity *U*, while radial coordinate is normalized with the exit pipe radius *R* ($r^*=r/R$). Tangential velocities in counter-clockwise direction are considered positive. Tangential velocity profiles have a typical trend with nearly linear inner region and inverse radius decay. The size of the linear inner zone according to the Rankine's and Burgers' vortex models, has been identified with the radial coordinate where the tangential velocity is maximum and it is almost the same at the different heights from the exit hole (equal to almost a half hole radius), while it increases slightly at higher flow rates, apart for S4 (Fig. 10a), probably because of the laser reflections on the strongly deformed free surface. The magnitude of the tangential velocity is larger when moving away from the hole, being at P3 more than three times larger than at P1. This indicates that the vortex rotation at free-surface level is predominant over the sink effect and involves a region with a radius larger more than four times the hole radius. On the other hand, as the flow rate increases at a given distance from the hole, the normalized maximum tangential velocity decreases, thus indicating that the additional kinetic energy is transferred to turbulent fluctuations. The same behaviors have been detected for the other tests with different Reynolds numbers or measurement plane heights, not shown here.

The average statistical error of tangential velocities is about 1%, with a maximum of 9.4% near the vortex center.

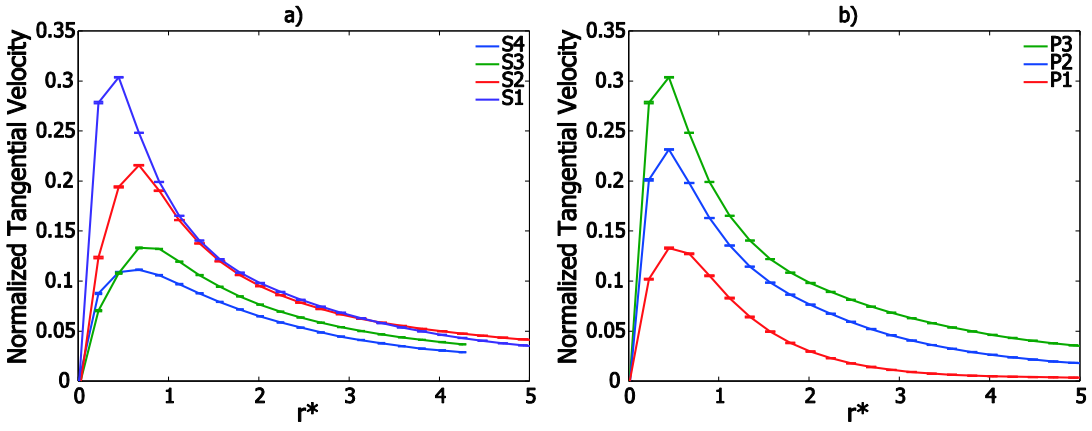

Fig. 10 Normalized tangential velocity profiles: **a)** at P3 and different Reynolds numbers; **b)** for S1at different planes

The previous experimental tangential velocity profiles are all very close to the potential decay typical of the Rankine vortex model:

$$u_\theta = \frac{\Gamma}{2\pi r} \tag{10}$$

where Γ is the vortex circulation. In Fig. 11, comparisons of experimental and analytical profiles at P3 (Fig. 11a) and for S1 at different planes (Fig. 11b) are shown. For each case, the circulation has been computed from PIV data as described in the next section. In Fig. 11a, there is a very good agreement between the potential behavior predicted by Rankine and the experimental profiles at P3 for all flow rates. On the other hand, the potential solution is approached much worse for measurements close to the exit hole, so that the potential flow approximation seems to be valid only on planes close to the free surface.

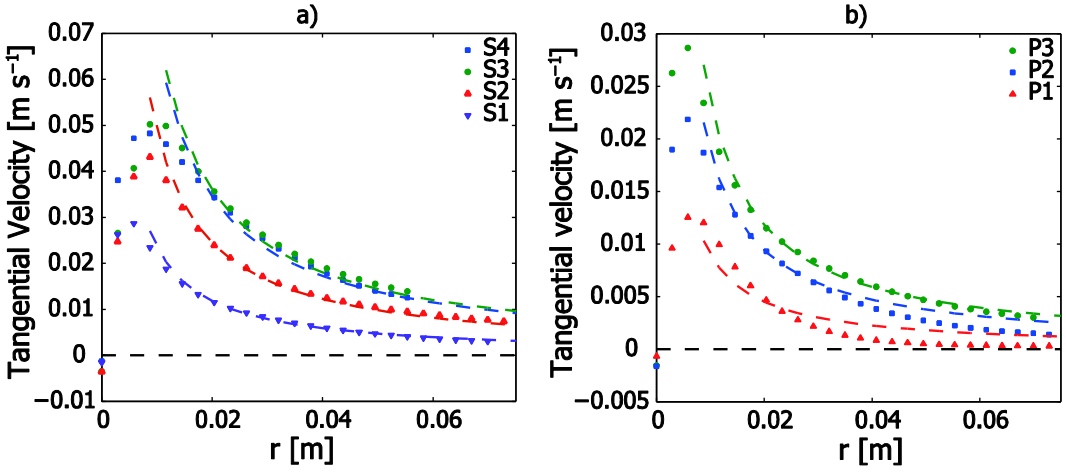

Fig. 11 Tangential velocity profiles compared with Rankine model, dotted lines: **a)** at P3 and different Reynolds numbers; **b)** S1at different planes

3.2.4. Vortex circulation

As previously stated, it is possible to compute the circulation from the tangential velocity on a closed path, *C*, surrounding the vortex and then the vortex size in the different experimental conditions. The circulation is a measure of vortex strength and it is related to the vorticity component orthogonal to the plane ω_z through

$$\Gamma = \oint_C \vec{U} \cdot d\vec{l} = \int_S \omega_z \, dS \tag{11}$$

where *S* is the surface in the horizontal plane enclosed by *C* and $d\vec{l}$ is an elementary path on *C*. In Fig. 12, the non-dimensional circulation (Γ/UD), evaluated on closed circular paths of increasing radius around the vortex center, are reported for different flow rates. The figure refers to planes P2 (Fig. 12a) and P3 (Fig. 12b). Theoretically, for a potential vortex, the circulation

should increase in the almost rigid vortex core and then it should reach a constant value in the potential external region. The experimental results roughly confirm this behavior, even if near to the hole (Fig. 12a) the constant value is not evident, as expected from the already noticed departure of tangential velocity profiles from potential theory in this region. Increasing the flow rate, the maximum dimensionless circulation decreases, whereas the position at which this is reached slightly increases.

The circulation curves are presented in Fig. 13a and Fig. 13b, respectively for cases S1 and S3, from which it is even more clear the departure from an external constant value when moving closer to the hole. In this region, the trend approaches a $1/r$ law, which indicates that velocity decays faster than $1/r$, *i.e.* approaching $1/r^2$, as also observed in the previous tangential plots (Fig. 11b). Increasing the vertical distance from the hole, the maximum non dimensionless circulation increases too, as the position at which this is reached. It is interesting to observe that the increase of vortex core circulation is almost linear in all the cases, while it should be non-linear if a linear behavior of the tangential velocity was attained in the core. Therefore, some additional effects in this region should be expected.

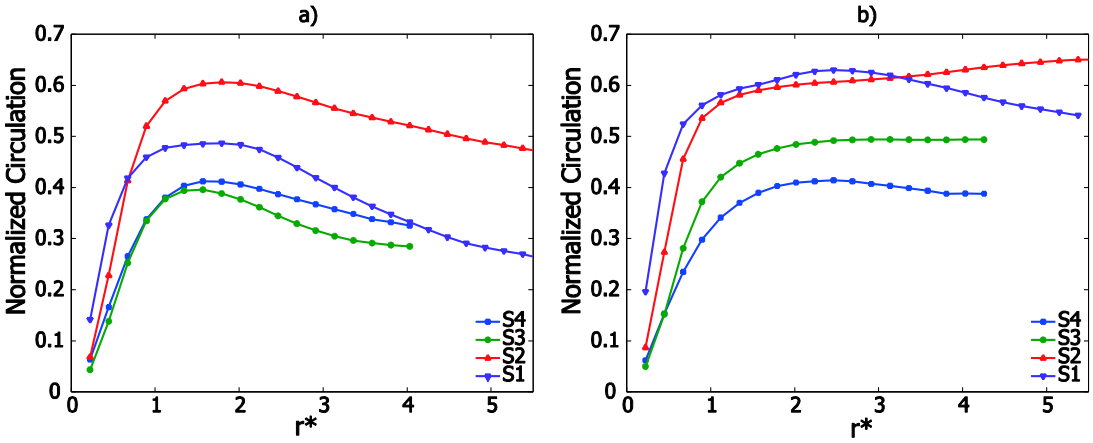

Fig. 12 Normalized circulation profiles for different flow rates: **a)** at P2; **b)** at P3

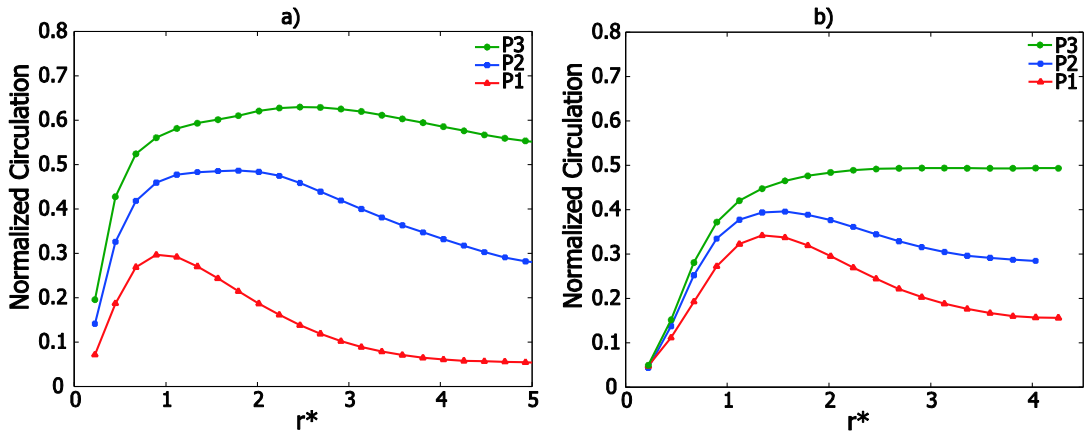

Fig. 13 Normalized circulation profiles for: **a)** S1; **b)** S3

3.3. Second-order moments

To investigate how the energy is transferred into velocity fluctuations, the root mean square (RMS) values of each fluctuating velocity component, non-dimensional by the exit velocity *U*, have been computed as:

$$u_r^{'} = \sqrt{\frac{\sum_{i=1}^{N}\left(u_{r_i}(x,y,t) - \overline{u_r}(x,y)\right)^2}{N}} \qquad u_\theta^{'} = \sqrt{\frac{\sum_{i=1}^{N}\left(u_{\theta_i}(x,y,t) - \overline{u_\theta}(x,y)\right)^2}{N}} \tag{12}$$

In Fig. 14 contours of radial velocity fluctuation RMS are shown at the plane P1. The largest fluctuations, about 1/10th of the exit velocity, are found at the vortex center as a result of both oscillations in vortex position and velocity variations related to the activation and pulsation of the bathtub vortex. For the case S2P1 there is also evidence of a double peak at the vortex center, probably caused by the lens effect as discussed for Fig. 7.

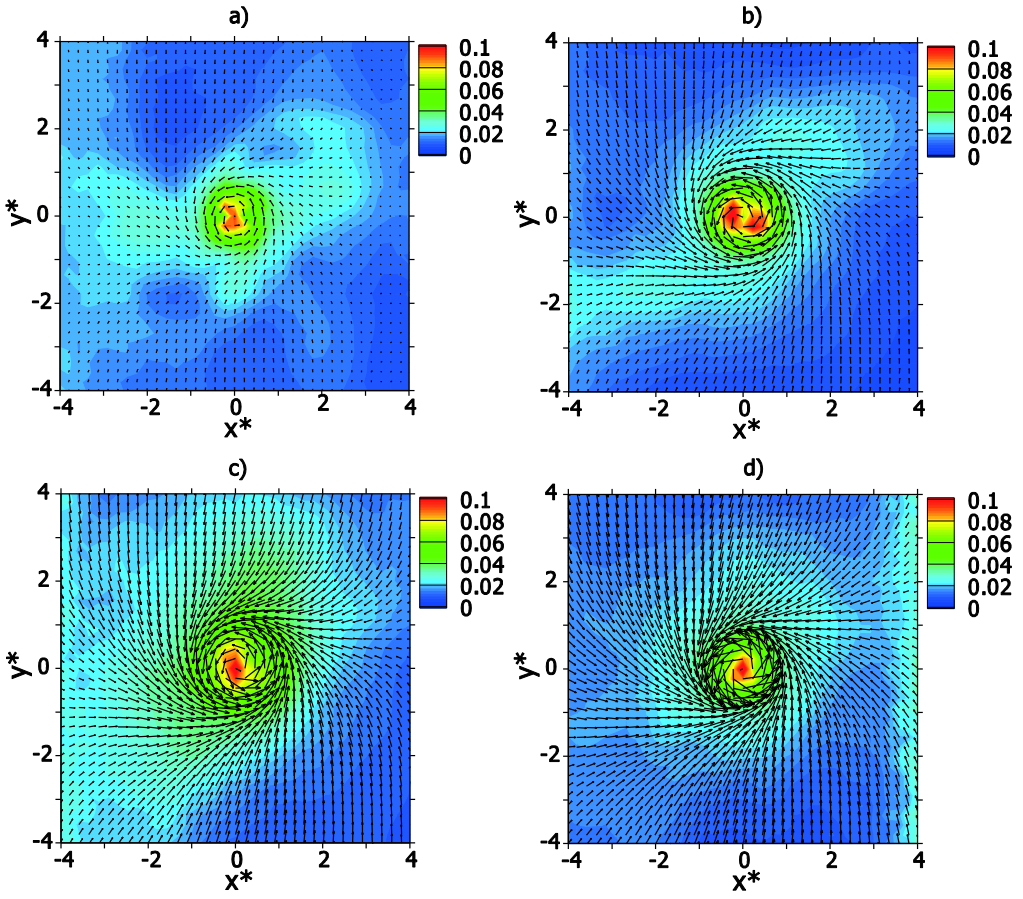

Fig. 14 Normalized radial velocity fluctuations RMS at P1 and different Reynolds numbers: **a)** S1; **b)** S2; **c)** S3; **d)** S4

Radial RMS velocity profiles are shown in Fig. 15, at P1 at different Reynolds numbers (Fig. 15a) and for S4 cases (Fig. 15b). It is quite clear that the intensity of non-dimensional

fluctuations is almost independent from the flow rate, thus establishing that the radial velocity fluctuations scale almost linearly with the velocity and the flow rate. For different planes, radial RMS profiles show similar trends and only at P3 there is a large peak at $r^*=0$, probably caused by the aforementioned reflections effects and free surface deformation problems near the vortex axis.

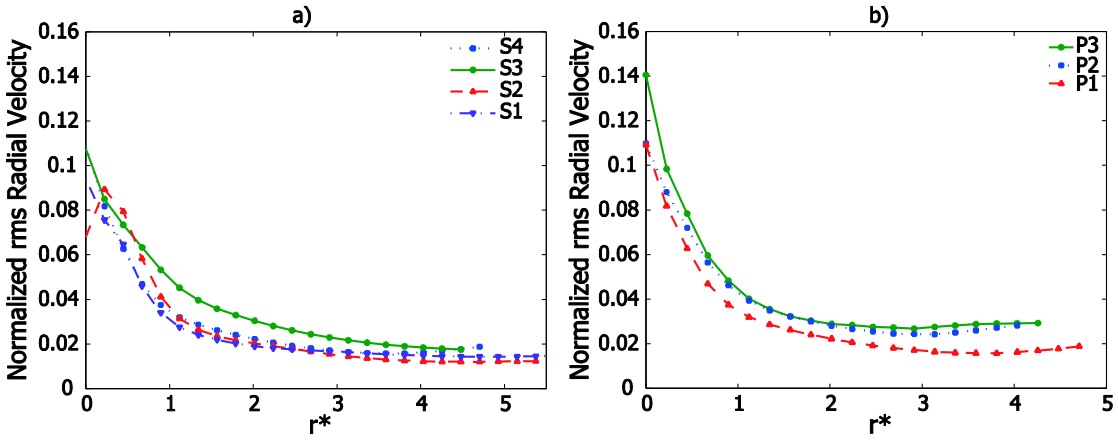

Fig. 15 Profiles of normalized radial velocity fluctuations RMS: **a)** at P1 and different Reynolds numbers; **b)** for S4 at different heights

Non-dimensional RMS values of the tangential velocity component present trends and values similar to those of the radial velocity; the fluctuations intensity decreases at higher flow rates. The Fig. 16a and the Fig. 16b show tangential RMS velocity profiles, respectively, at P1 and for S2. Here (Fig. 16b), the evidence of a peak is larger than in the radial RMS velocity plots, especially for the lower flow rates. This suggests that large velocity fluctuations are located just around the vortex center, where there is the tangential velocity maximum. As before, the RMS profiles reach similar levels at different flow rates, whereas it is evident (Fig. 16b) that the intensity of tangential velocity fluctuations increases for planes approaching the free surface. These behaviors could be explained assuming that by increasing the flow rate there is an increasing amount of kinetic energy transferred to turbulent fluctuations, as it happens also moving towards the free surface, where the radial component of velocity tends to vanish; however, measurements of the axial velocity are needed to confirm this increased energy transfer at large flow rates.

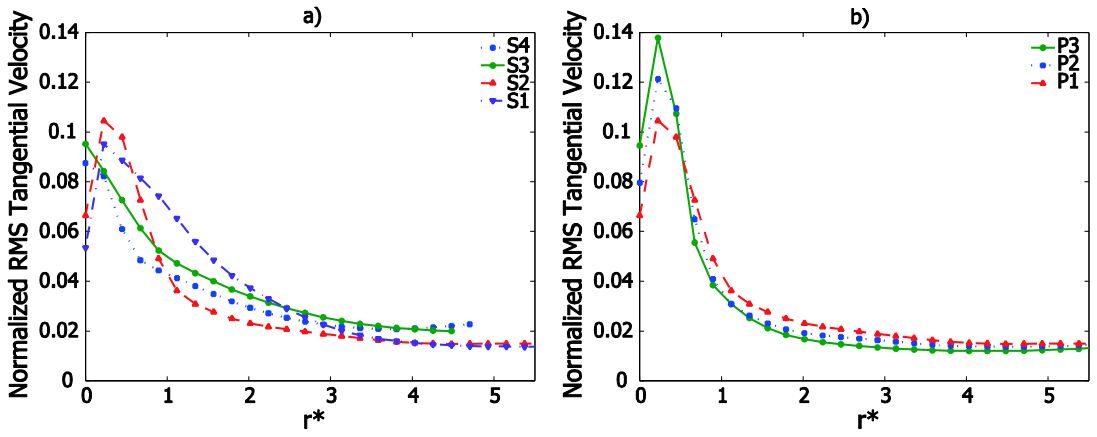

Fig. 16 Profiles of normalized tangential velocity fluctuations RMS: **a)** at P1 and different Reynolds numbers; **b)** for S2 at different planes

4. Conclusions

The aim of this work was to characterize the flow field and the structure of the unforced free surface vortices, performing PIV measurements at three horizontal planes and for different vortex stages. Observed vortices, generated without imposing any forced rotation, were characterized by a consistent variation of their position and intensity during the measurement period and, as a consequence, the vortex center of each instantaneous velocity field was determined before calculating averaged velocity fields. Vortex trajectories show an increasing radius of the orbital motion around the hole, as the distance from the exit hole increased. The radius also increases with the flow rate, showing a more irregular trajectory.

Normalized radial profiles acquired close to the exit hole are very close one to each other, thus exhibiting a good scaling behavior, when using the average exit fluid velocity as scaling velocity. In this region, the decay along the radius appears very similar to that derived from the potential flow solution. Therefore, in an unforced vortex, the radial flow is governed predominantly by the exit fluid velocity and can be considered as potential near the exit hole, while it gradually fades moving towards the free surface. Tangential velocity profiles have a typical trend with a nearly linear inner region and an inverse radius decay; the linear inner zone size (equal to about one half of the hole radius) is almost the same at the different planes, while it increases slightly for large flow rates. The magnitude of the tangential velocity is larger when moving away from the hole, thus indicating that the rotational motion at free-surface is predominant over the sink effect and involves a larger region. On the other hand, as the flow rate increases at a given distance from the hole, the normalized maximum tangential velocity decreases, thus indicating that the additional kinetic energy is transferred to turbulent

fluctuations. The potential flow approximation (Rankine vortex model) for tangential velocity seems to be valid only on planes close to the free surface. Therefore, the analytical vortex model, based on the hypothesis of potential flow, can be applied to describe the flow of unforced vortices only near the free surface. The potential behaviors of radial and tangential profiles, respectively near the exit hole and near the free surface, could be used as boundary conditions to develop more reliable analytical vortex models.

Starting from average velocity fields, the circulation profiles were calculated. Experimental circulation profiles for planes close to the free surface roughly also confirm the potential behavior, with an initial increasing near the vortex center, and then a constant value in the potential outer region. Increasing the flow rate, the maximum dimensionless circulation decreases, whereas the position at which this is reached slightly increases. On the other hand, circulation profiles at measurement planes close to the exit hole show a departure from the potential trend (as for tangential velocity profiles). Increasing the distance from the hole, the maximum normalized circulation also increases.

The root mean square (RMS) values of each velocity component have been computed to evaluate how the energy is transferred into velocity fluctuations. The largest fluctuations, around $1/10^{th}$ of the exit velocity, are found at the vortex center as a result of both oscillations in vortex position and velocity variations related to the activation and pulsation of the bathtub vortex.

The present results can be used as reference to validate different analytical models and to determine which model is able to describe more accurately the structure of an unforced vortex. Furthermore, experimental data could be used to validate numerical results, obtained from CFD simulations, in order to choose the most suitable numerical scheme and model for the simulation of free surface vortices.

PIV measurements of the flow field of forced vortices, which are generated by imposing tangential inlets to the fluid, are currently ongoing. The comparison of the forced and free bathtub vortices flow fields will be important to highlight the influence of a promoted rotation on the vortex structure.

References

[1] Lungt H J (1983) Vortex flow in nature and technology. New York, USA: Wiley-Interscience

[2] Tenchine D (2010) Some thermal hydraulic challenges in sodium cooled fast reactors. Nucl Eng Des 240 (5): 1195–1217

[3] Rankine W J M (1858) Manual of Applied Mechanics. Griffin, London

[4] Burgers J M (1948) A mathematical model illustrating the theory of turbulence. Adv In Appl Mech: 171-199 (New York:Academic Press)

[5] Rosenhead L (1930) The spread of vorticity in the wake behind a cylinder. Proc. Royal Society London, England, Series A, 127: 590-612

[6] Hite E J, Mih W C (1994) Velocity of vertical vortices at hydraulic intakes. J Hydr Eng ASCE 120 (3): 284-297

[7] Chen Y I, Wu C, Ye M, Ju X (2007) Hydraulic characteristics of vertical vortex at hydraulic intakes. J Hydrodyn 19 (2): 143–149

[8] Lundgren T S (1985) The vortical flow above the drain-hole in a rotating vessel. J Fluid Mech 155: 381–412

[9] Andersen A, Bohr T, Stenum B, Jull Rasmussen J, Launtrup B (2006) The bathtub vortex in a rotating container. J Fluid Mech 556: 121-146

[10] Batchelor G K (1967) An introduction to Fluid Dynamics. Cambridge University Press, Cambridge

[11] Stepanyants Y A, Yeoh G H (2008) Stationary bathtub vortices and a critical regime of liquid discharge. J Fluid Mech 604: 77-98

[12] Stepanyants Y A, Yeoh G H (2008) Burgers-Rott vortices with surface tension. J Appl Math Phys (ZAMP) 59: 1-12

[13] Gulliver J S, Rindels A J (1987) Weak vortices at vertical intakes. J Hydr Eng ASCE 113 (9): 1101-1116

[14] Baum M R, Cook M E (1974) Gas entrainment at the free surface of a liquid: entrainment inception at a laminar vortex. J Brit Nucl Eng Soc 13: 203-209

[15] Caruso G, Cristofano L, Nobili M, Vitale Di Maio D (2014) Experimental investigation of free surface vortices and definition of Gas Entrainment occurrence maps. J Phys Conf Ser 501, 012019. doi:10.1088/1742-6596/501/1/012019

[16] Cristofano L, Nobili M, Caruso G (2014) Experimental study on unstable free surface vortices and gas entrainment onset conditions. Exp Therm Fluid Sci 52: 221-229

[17] Sakai T, Eguchi Y, Monji H, Ito K, Ohshima H (2008) Proposal of design criteria for gas entrainment from vortex dimples based on a computational fluid dynamics method. Heat Transfer Eng 29: 731-739

[18] Ito K. Kunugi T, Ohshima H, Kawamura T (2009) Formulations and validations of a high-precision volume-of-fluid algorithm on nonorthogonal meshes for numerical simulations of Gas Entrainment phenomena. J Nucl Sci Technol 46: 366-373

[19] Merzari E, Ninokata H, Wang S, Baglietto E (2009) Numerical simulation of free-surface vortices. Nucl Technol 165: 313-320

[20] Škerlavaj A, Lipej A, Ravnik J, Škerget L (2010) Turbulence model comparison for a surface vortex simulation. IOP Conf Ser: Earth Environ. Sci 12, 012034

[21] Škerlavaj A, Škerget L, Ravnik J, Lipej A (2014) Predicting free-surface vortices with single-phase simulations. Eng Appl Comp Fluid 8 (2): 193-210

[22] Monji H, Shinozaki T, Kamide H, Sakai T (2010) Effect of experimental conditions on gas core length and downward velocity of free surface vortex in cylindrical vessel. J Eng Gas Turb Power 132 (1), 012901

[23] Cristofano L, Nobili M, Caruso G (2014) Numerical evaluation of gas core length in free surface vortices. J Phys: Conf Ser 547, 012030. doi:10.1088/1742-6596/547/1/012030

[24] Noguchi T, Yukimoto S, Kimura R, Niino H (2003) Structure and instability of a sink vortex. Proc. PSFVIP-4, Chamonix, France

[25] Kimura N, Ezure T, Tobita A, Kamide H (2008) Experimental study on gas entrainment at free surface in reactor vessel of a compact sodium-cooled fast reactor. J Nucl Sci and Tech 45: 1053-1062

[26] Li H, Chen H, Ma Z, Zhou Y (2008) Experimental and numerical investigation of free surface vortex. J Hydrodyn Ser B 20 (4): 485-491

[27] Cristofano L, Nobili M, Romano G P, Caruso G (2014c) Velocity profiles in bathtub vortices: validation of analytical models. 32nd UIT Heat Transfer Conference, Pisa

[28] Hunt J C R, Wray A A, Moin P (1988) Eddies, stream, and convergence zones in turbulent flows. Center for Turbulence Research Report CTR-S88: 193–208

Title: Investigation on bathtub vortex flow field by Particle Image Velocimetry

Highlights:

- A Particle Image Velocimetry investigation on bathtub vortices has been carried out
- Velocity and vorticity fields at different planes and Reynolds numbers were obtained
- Radial and tangential velocity profiles have been compared with the potential flow
- Turbulence fluctuations analysis of the vortex motion and velocity fields is included